ADVANCES IN ATMOSPHERIC SCIENCES, VOL. 32, MAY 2015, 624–634

Identification and Analysis of High-Frequency Oscillations in the Eyewalls of Tropical Cyclones

CHEN Shumin[1,2], Youyu LU[3], LI Weibiao*[1], and WEN Zhiping[1]

[1]*Department of Atmospheric Sciences, Sun Yat-Sen University, Guangzhou* 510275

[2]*State Key Laboratory of Tropical Oceanography, South China Sea Institute of Oceanology, Chinese Academy of Sciences, Guangzhou* 510301

[3]*Bedford Institute of Oceanography, Fisheries and Oceans Canada, Dartmouth, Nova Scotia, B2Y 4A2 Canada*

(Received 8 April 2014; revised 22 August 2014; accepted 15 September 2014)

ABSTRACT

High-frequency oscillations, with periods of about 2 hours, are first identified by applying wavelet analysis to observed minutely wind speeds around the eye and eyewall of tropical cyclones (TCs). Analysis of a model simulation of Typhoon Hagupit (2008) shows that the oscillations also occur in the TC intensity, vertical motion, convergence activity and air density around the eyewall. Sequences of oscillations in these variables follow a certain order.

Key words: tropical cyclone, high-frequency oscillations, eyewall, intensity

Citation: Chen, S. M., Y. Y. Lu, W. B. Li, and Z. P. Wen, 2015: Identification and analysis of high-frequency oscillations in the eyewalls of tropical cyclones. *Adv. Atmos. Sci.*, **32**(5), 624–634, doi: 10.1007/s00376-014-4063-x.

1. Introduction

Tropical cyclones (TCs) are one of the most energetic weather phenomena and pose great scientific challenges to meteorologists. Although forecasting of TC tracks has significantly improved (Emanuel, 1999, 2000), accurate prediction of TC intensities is still difficult (Wang and Chan, 2002; Knapp and Kruk, 2010; DeMaria et al., 2014).

TCs are complex systems and their intensities are affected by a variety of physical processes. Many studies focus on the TC's updraft and the eyewall-produced updraft. One aspect is the updraft's control of TC intensity through the activity of secondary circulation. This is related to the positive feedback mechanisms for the genesis and maintenance of TCs, for which there are two classical theories: "conditional instability of second kind" (CISK; Charney and Elliassen, 1964) and "wind-induced surface heat exchange" (WISHE; Emanuel, 1986; Rotunno and Emanuel, 1987; Emanuel, 1989, 1997). The other aspect is related to the structure and activities in the eyewall. This includes mesoscale convective systems (MCSs; Hendricks et al., 2004; Montgomery et al., 2006, 2009), secondary rain bands (e.g., Montgomery and Kallenbach, 1997; Reasor et al., 2000), eyewall cycles (Shapiro and Willoughby, 1982) and activities of waves.

Studies on waves in the eyewall generally focus on the vortex Rossby waves (Chen et al., 2003; Zhong et al., 2009; Menelaou and Yau, 2014), inertia gravity waves (Willoughby, 1976; Kurihara, 1976; Schecter, 2008; Ki and Chun, 2011), and the fine-scale spiral rainbands, which are associated with Kelvin–Helmoltz instability (Romine and Wilhelmson, 2006) and inertial-buoyancy waves (Li et al., 2010). However, these sorts of studies generally focus on the horizontal distribution and propagation of the waves. The temporal evolution of the waves and their vertical propagation have not been fully investigated.

In this study, the activities of waves are analyzed with a focus on the temporal evolution and vertical propagation. Evidence of high-frequency oscillations, with periods of about 2 hours, is revealed from analysis of observed wind speeds and model-simulated TCs. Such high-frequency oscillations have not been reported in previous studies, probably due to the lack of available *in-situ* high-frequency observations in the central areas of TCs.

2. Analysis procedure

The characteristics of high-frequency oscillations in the eyewall of TCs are analyzed by applying the wavelet transform to both the observations and the outputs from a numerical simulation.

2.1. *Observational data at Shangchuan Station*

Minutely wind speed and surface pressure from the automatic weather station at Shangchuan (21.7°N, 112.8°E) are used in this study. The station is located in the central part of

* Corresponding author: LI Weibiao
Email: eeslwb@mail.sysu.edu.cn

Shangchuan Island at an elevation of 83 m above sea level. The data are collected and quality controlled by the Climate Center of Guangdong Province. Shangchuan Island is one of the largest islands in Guangdong Province and is also a region heavily influenced typhoons.

2.2. *Model simulation*

Because the observations are insufficient for capturing the detailed characteristics of TCs, we also analyze the TC simulated by a numerical model. The simulation is based on the Weather Research and Forecasting (WRF) model (Skamarock et al., 2008) developed for advancing the study and prediction of mesoscale weather and accelerating the transfer of research advances into operation. The Advanced Research WRF (ARW) dynamics solver integrates the compressible non-hydrostatic Euler equations that are cast in flux forms. The equations are formulated using a terrain-following hydrostatic-pressure (σ) coordinate in the vertical direction. The horizontal discretization uses the Arakawa-C staggering grids. The WRF physical processes include a selection of explicit microphysics schemes, cumulus convective parameterizations, a land-surface model, planetary boundary layer (PBL) parameterizations, and longwave and shortwave radiation schemes.

2.3. *The wavelet transform*

The wavelet transform, following Christopher and Compo (1998), is applied to the observations and model output. For a time series denoted by $b_k\,(k = 0, 1, \ldots, N-1)$, the wavelet transform decomposes the signal into scaled and translated versions of a "mother wavelet" Ψ_0, resulting in "child wavelets", or simply "wavelets", represented by

$$\Psi_{S_j,k} = \left(\frac{\delta t}{s_j}\right)^{1/2} \Psi_0\left[\frac{(-n)\delta t}{s_j}\right], \qquad (1)$$

where s_j and n represent scale and translation (on the time axis), respectively; δt represents the sampling period of the signal; and $(\delta t/s_j)^{1/2}$ represents the energy normalization factor that keeps the energy of child wavelets the same as that of the mother wavelet. The signal is then converted to the scale and translation domains by scaling and translating the mother wavelet to match the high and low frequencies in the signal, thus providing an improved fitting to the data. This process is represented by a convolution of x_k with the scaled and translated wavelets:

$$W(n,s_j) = \sum_{k=0}^{N} b_k \Psi^*_{s_j,n}(k)\,, \qquad (2)$$

where the asterisk denotes the complex conjugate and $W(n,s_j)$ is called a wavelet coefficient. The wavelet power spectrum (WPS) is defined as $|W(n,s_j)|^2$; and the significance levels of $W(n,s_j)$ can be determined by the wavelet red noise spectrum, with details provided by Christopher and Compo (1998). The normalized WPS (NWPS) describes the contribution of a certain scale to the total energy. Following Zhu et al. (2010), the NWPS $E(n,s_j)$ is defined as

$$E(n,s_j) = \frac{|W(n,s_j)|^2}{\sum_{j=1}^{J}|W(n,s_j)|^2}\,. \qquad (3)$$

3. Observational facts

We first analyze the wind speeds and surface pressure during three TCs, with a sampling period of 1 minute, observed at Shangchuan Station. The three TCs are: Severe Typhoon Hagupit (2008), Severe Tropical Storm Goni (2009), and Typhoon Koppu (2009). They passed through Shangchuan Station at 0000 UTC 24 September 2008, 0000 UTC 5 August 2009, and 1800 UTC 14 September 2009, respectively. Figure 1 shows the observed tracks and maximum wind speed (MWS) of these TCs, taken from the CMA-STI best-track

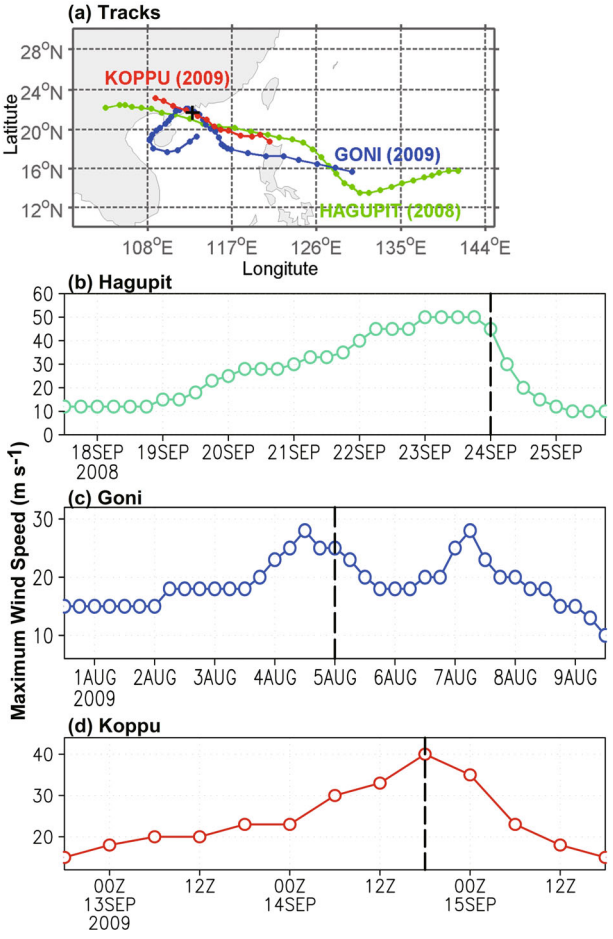

Fig. 1. (a) Tracks and (b–d) intensities of Severe Typhoon Hagupit (2008, green), Severe Tropical Storm Goni (2009, blue) and Typhoon Koppu (2009, red) from the CMA-STI best-track data. In (a), solid dots show the positions of the TC center at every 6 hours, and the black cross denotes the location of the automatic weather station at Shangchuan (21.7°N, 112.8°E). In (b–d), the TC intensities are represented by the 6-hourly maximum wind speed (units: m s^{-1}), with black dashed lines denoting the time when the TCs passed through Shangchuan Station.

dataset (Ying et al., 2014) for TCs complied by the Shanghai Typhoon Institute (STI), China Meteorological Administration (CMA). The location of Shangchuan Station and the times that the TCs passed through the station are also shown in Fig. 1. The wavelet transform is applied to the time series of the wind speeds and pressures covering 24 hours, including 12 hours before and after the TCs passed the station. The analysis results for the wind speeds are shown in Fig. 2. Denoted by the gray shading, and the contours of 10%, the spectral energy is significant at periods of about 2 hours: 90–120 minutes for Hagupit (2008), 90–150 minutes for Goni (2009), and 75–150 minutes for Koppu (2009). Based on the relationship between the periods and discrete scales given in Christopher and Compo (1998), the period of 2 hours corresponds to a spatial scale of about 10 km. This aspect is discussed in section 5. Judging from the shaded area in Fig. 2, these high-frequency oscillations are usually significantly different from the red-noise process around the eye and eyewall where winds are strong. In asymmetric TCs [Hagupit (2008) and Koppu (2009)], the oscillations are more significant at the side with higher wind speeds.

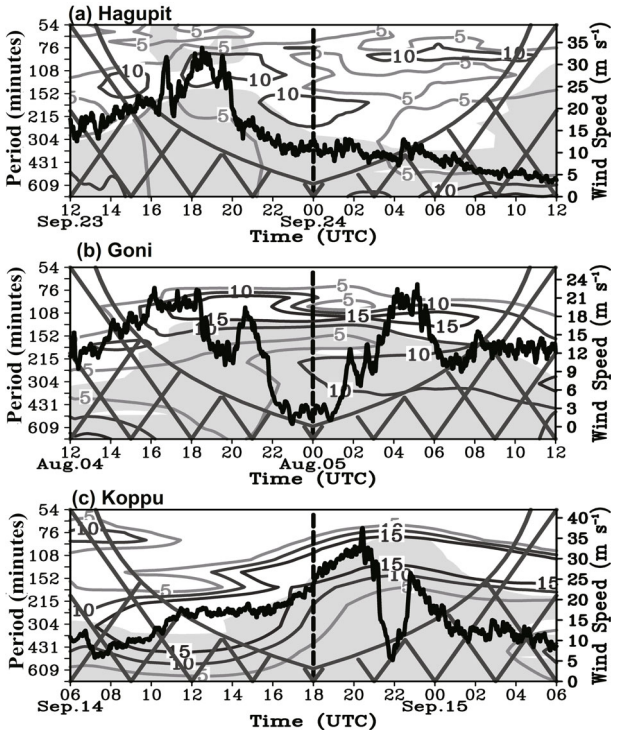

Fig. 2. Time series of the minutely wind speeds observed at Shangchuan Station (black curves; units: m s^{-1}), with magnitude denoted by the axis on the right-hand side; and the normalized wavelet power spectrum (NWPS; contours; units: %) of these time series. Panels (a–c) are for Hagupit (2008), Goni (2009) and Koppu (2009), respectively. The left-hand axis is the Fourier period (in minutes) corresponding to the wavelet scale. Gray shading indicates the time and periods within which the wavelet power spectrum (WPS) is significantly different from that of a red-noise process at the 0.05 confidence level. Cross-hatched regions indicate the "cone of influence" where edge effects become important. The black dashed lines denote the time when the TCs passed through Shangchuan Station.

Figure 3 shows the NWPS of the observed minutely wind speed and pressure at Shangchuan Station, integrated for variations at time scales of 90–150 minutes. Figures 3a–c show the 24-hour durations when the three TCs passed the station. For reference, the NWPS during a period of 24 hours without TC activity is shown in Fig. 3d. The high-frequency oscillations are significant in the wind speeds under TC conditions, which boost the maximum NWPS by at least 10%–20%. Compared with winds, the high-frequency oscillations in the pressure are insignificant, the reasons for which are discussed in section 5.

The spectral energy is also significant in the range of periods of about 3–6 hours (Fig. 2). Such variations represent the evolution of wind speed due to different parts of the TC passing by the station. These include: the outer region with relatively weak winds, the eyewall with strong winds, and the eye with nearly static wind. As the outer region and eyewall of one side, the eye, and then the eyewall and outer region of the other side pass through the station successively, the wind speeds observed at the station increase and decrease accordingly.

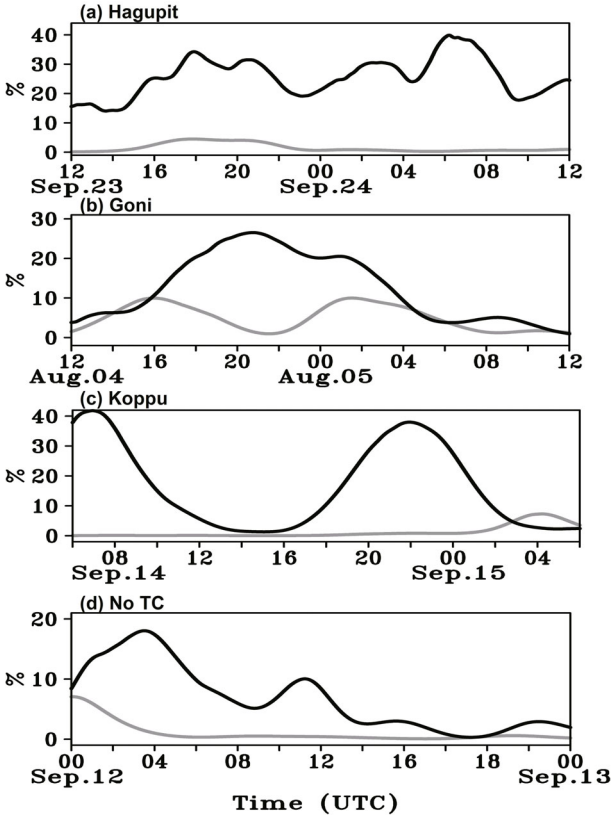

Fig. 3. The integrated NWPS (%) of the observed minutely wind speed (black) and pressure (gray) at Shangchuan Station, computed by integrating the NWPS over time scales of 90–150 minutes. Panels (a–c) are for Hagupit (2008), Goni (2009) and Koppu (2009), respectively. Panel (d) represents the NWPS of the 24 hours without TC activity.

4. Model experiments

4.1. *Experiment setup*

The WRF model is applied to simulate Typhoon Hagupit. The model includes three fixed two-way interactive domains on Mercator projections (Fig. 4), with detailed parameters provided in Table 1. Domain 1, the outer mesh, has a horizontal resolution of 27 km, and is designed to simulate the synoptic-scale environment for the storm to evolve. Domain 2 has a resolution of 9 km, and is designed to simulate the mesoscale structure of Hagupit. Domain 3, the inner mesh, has a resolution of 3 km, and is designed to simulate the inner-core structure of Hagupit. There are 28 unevenly spaced vertical levels with a higher resolution in the PBL. The top is set to 50 hPa. The σ levels are placed at values of 1.000, 0.990, 0.978, 0.964, 0.946, 0.922, 0.894, 0.860, 0.817, 0.766, 0.707, 0.644, 0.576, 0.507, 0.444, 0.380, 0.324, 0.273, 0.228, 0.188, 0.152, 0.121, 0.093, 0.069, 0.048, 0.029, 0.014, and 0.000. Apart from the cumulus parameterization scheme not being used in Domain 3, the physical schemes are the same for the sub-models of the three domains. The Kain–Fritsch (KF) cumulus parameterization scheme (Kain and Fritsch, 1990, 1993; Kain, 2004) is used because it provides the best result based on tests of various cumulus parameterization schemes for this case. Other options of model physics being used are the WRF Single-Moment 6-Class (WSM6) microphysics scheme (Hong et al., 2004), the Yonsei University (YSU) PBL scheme (Hong and Lim, 2006), the 5-layer thermal diffusion land-surface model scheme (Skamarock et al., 2008), the Rapid Radiative Transfer Model (RRTM) longwave radiation scheme (Mlawer et al., 1997), and the Dudhia shortwave radiation scheme (Dudhia, 1989).

The initial and boundary conditions are obtained from the 6-hourly US National Centers for Environmental Prediction (NCEP) Final Analysis (FNL) data. The SST is fixed during model integration. The analysis fields with a horizontal resolution of $1^\circ \times 1^\circ$, including temperature, wind, geopotential height, and dewpond at mandatory pressure levels, are interpolated horizontally to the horizontal points and vertically to the σ levels. The boundary conditions of the outermost domains are specified by temporally interpolating the NCEP FNL data. Each coarser domain provides the next finer domain with time-dependent lateral boundary conditions, while the solution of each finer domain feeds back to that of the next coarser domain at every time step. The two-way interactions among the sub-models of the three domains are thus achieved.

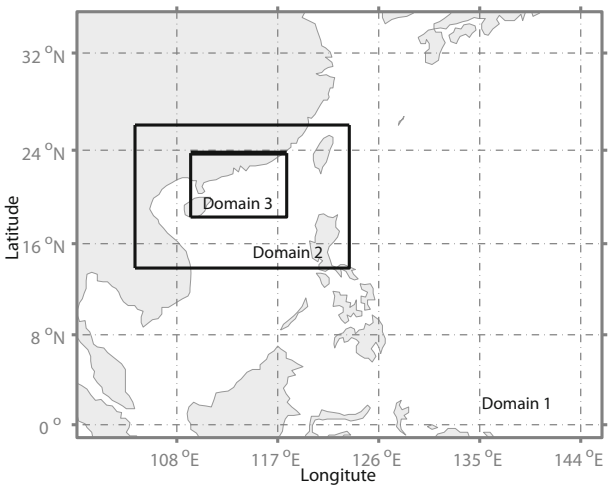

Fig. 4. The domain configuration of the model.

Table 1. Model setup parameters.

	Domain		
	1	2	3
Dimensions (x, y)	180×150	220×151	294×201
Grid size (km)	27	9	3
Time step (s)	50	16.67	5.56
Start time	1200 UTC 22 Sep	1200 UTC 22 Sep	0600 UTC 23 Sep
Integration hours	0–48	0–48	18–36

Because the first guess information is from the NCEP FNL data with relatively coarse resolution, the vortices contained are too broad and too weak. Initialization of a higher-resolution model with such coarse resolution fields only obtains the general physical characteristics of the storms. To improve the simulation of intensity, the initial vortex in the NCEP FNL data is replaced by a new vortex with intensity closer to observations using the NCAR-AFWA (Air Force Weather Agency) bogussing scheme (Davis and Low-Nam, 2001; Low-Nam and Davis, 2001). The following assumptions are made in defining the bogus storm profile: (1) axisymmetry; (2) vorticity specified within 300 km of the bogus storm center; (3) fixed radius of maximum wind (RMW); (4) mass and wind fields in nonlinear balance; (5) nearly saturated core without an eye; and (6) the maximum winds of the bogus storm being a pre-determined fraction of the observed maximum winds.

The simulation is initialized at 1200 UTC 22 September when the TC has crossed the Balintang Channel and entered the South China Sea, and has a relatively complete structure (figure not shown). A bogus vortex is introduced at the initializing time, with the center located at (19.5°N, 120.8°E) (the same as the center location in the best-track achieves), and the maximum wind speed is set to 70 m s^{-1} using an RMW of 81 km. Based on a large number of tests initialized with vortexes of different intensities, this bogus vortex provides the best result after the spin-up process. The integration is carried out for 48 hours, terminated at 1200 UTC 24 September, about 12 hours after Hagupit made landfall. The 48-hour integration covers the intensification, mature, and weakening stages of the life cycle of Hagupit.

4.2. *Model validations*

The model outputs from Domain 2, covering the intensification, mature, and weakening stages of the life cycle of Hagupit, are compared to observations. Figure 5 shows the observed (CMA-STI) and simulated TC tracks. Figure

6a shows the deviations of the simulated track from the observed track. During 0–36 hours of integration before the storm made landfall, the simulated track agrees well with the observed track, with less than 40 km discrepancy in the positions of the TC center. During the last 10 hours of integration after the storm made landfall, the discrepancy increases to about 80 km; the simulated storm is located to the north-northeast of the observed location. The discrepancy may be caused by inaccuracy in the simulation of the large-scale circulation or the terrain data in the WRF model.

Figures 6b and c compare the minimum sea level pressure and the maximum wind speed, respectively. Despite evident differences in the detail, the trends agree well. The simulation shows an initial adjustment in the first 15 minutes, followed by a relatively steady period. The rapid adjustment in the first few minutes may be due to the fact that the model does not account for friction in the PBL, and thus the prescribed nonlinear balance is disturbed (Low-Nam and Davis, 2001). From 4 hours to around 10 hours, the simulated sea level pressure keeps increasing while the maximum wind speed keeps decreasing. Such trends are not present in the best-track data. Li et al. (2013) attributed this discrepancy to the spin-up process of the model. During 19–36 hours, when the simulated and observed TCs both reach their strongest stage, the maximum surface wind speeds are nearly equal, although the simulated minimum sea level pressure is slightly lower.

The simulated 10 m wind speed and surface pressure are also compared with the hourly observations at three automatic weather stations, located in Heshan (22.8°N, 113.0°E), Shangchuan and Dianbai (21.4°N, 111.2°E). These stations were quite close to the storm center when Hagupit was about to make landfall (Fig. 5). Figure 7 compares the observed and

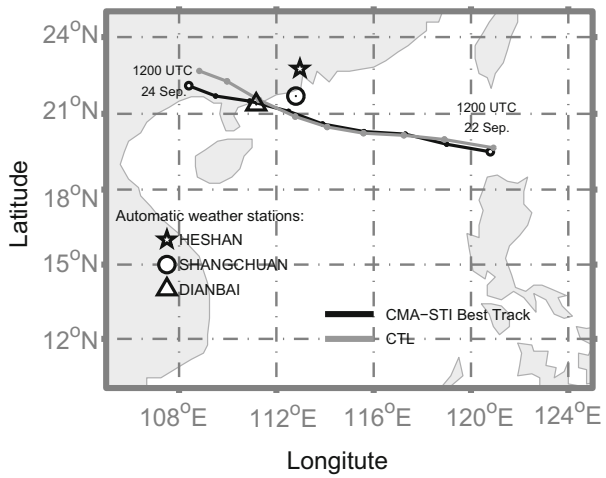

Fig. 5. Tracks of Typhoon Hagupit (2008) from observation (black) and simulation (gray). Open circles at each end of the observed track denote the position of the TC center at 1200 UTC 22 Sep (right) and 1200 UTC 24 Sep (left). Solid dots along the simulated track show the position of the TC center every 6 hours. The locations of the automatic weather stations at Heshan (22.8°N, 113.0°E), Shangchuan (21.7°N, 112.8°E) and Dianbai (21.4°N, 111.2°E) are represented by the star, the larger open circle, and the triangle, respectively.

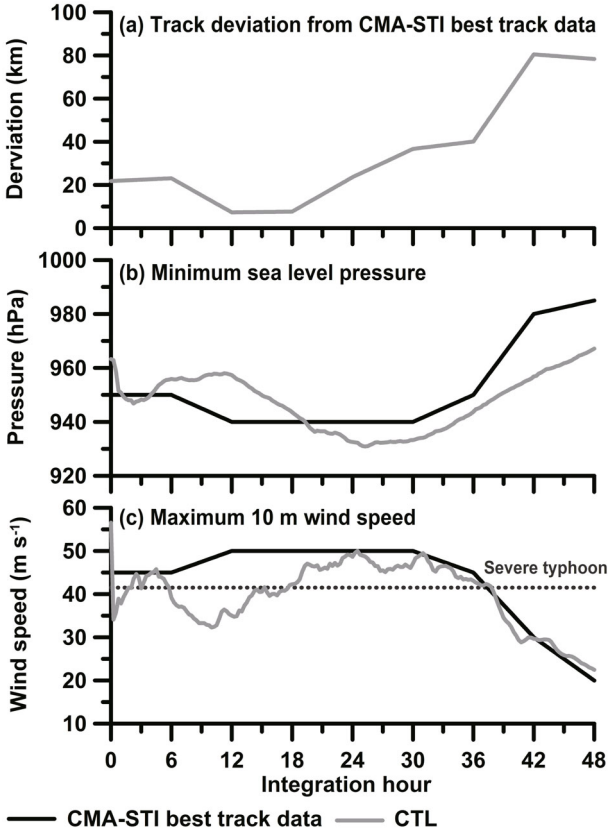

Fig. 6. Comparison of CMA-STI best-track data (black) with the model simulation (gray): (a) deviations of the simulated track from the CMA-STI best-track data; (b) the minimum sea level pressure (central pressure; units: hPa); and (c) the maximum 10 m wind speed (m s^{-1}), with the dashed line denoting the lowest maximum wind speed for the severe typhoon.

simulated pressure and 10 m wind speed. In general, the observed and simulated time variations are consistent, although the simulated evolution lags the observed one by nearly 2 hours. Furthermore, the simulated wind speed and surface pressure are also consistent with the minutely observations at Shangchuan Station (Fig. 8). As given in Fig. 8c, the NWPS of the simulated 10 m wind speed and surface pressure are similar to the minutely observations (Fig. 3a).

Shifting attention to the system-scale features, Fig. 9 compares the simulated grid-scale precipitation with the Tropical Rainfall Measuring Mission (TRMM) Microwave Imager (TMI) 2A12 surface rain rate. The TMI profiling algorithm (2A12) generates vertical profiles of hydrometeors from TMI brightness temperatures, through blending the radiometric data with dynamical cloud models. For each pixel, the algorithm assigns a surface type (land/ocean/coast) and a freezing height; and computes surface rain, convective surface rain, and profiles of hydrometeors (cloud liquid, cloud ice, water vapor etc.) at 14 vertical levels. Figure 9 shows that the simulation obtains intense precipitation, similar to observations, though it overestimates the magnitudes by a factor of two. The reason is that TRMM tends to underestimate moderate to high rains (> 50 mm h^{-1}), although it has superior

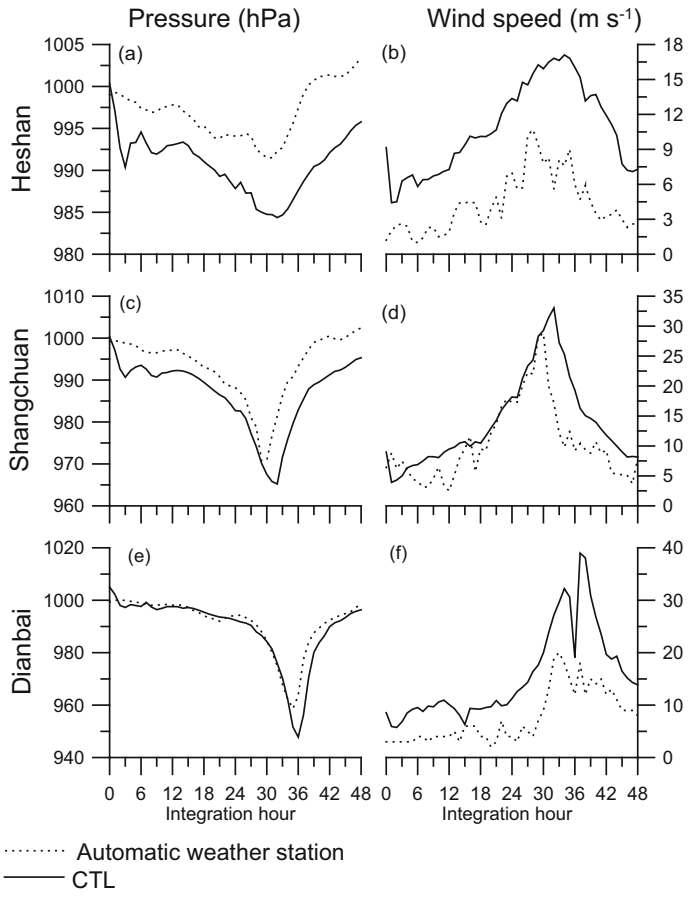

Fig. 7. Hourly time series from observations (dashed lines) and the model (solid lines) for surface pressure (left column; units: hPa) and wind speed (right column; units: m s^{-1}) at (a, b) Heshan, (c, d) Shangchuan, and (e, f) Dianbai. The locations of the stations are shown in Fig. 5.

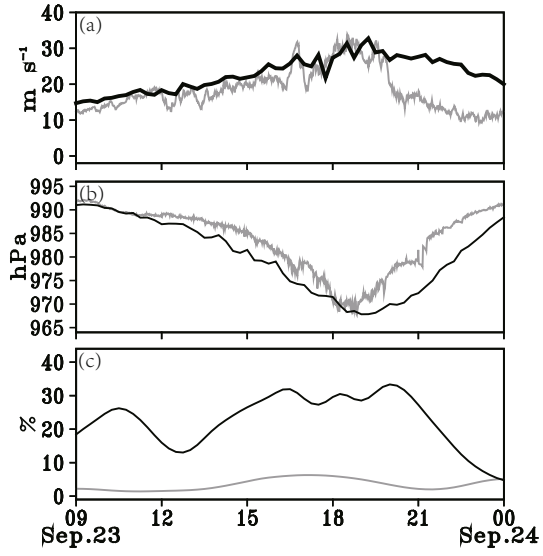

Fig. 8. Minutely time series from observations (gray) and the model (black) for (a) wind speed (units: m s^{-1}) and (b) surface pressure (units: hPa). (c) The NWPS (units: %) integrated for variations at time scales of 90–150 minutes of the simulated wind speed (black) and pressure (gray). All times are from the location of Shangchuan Station.

skill in detecting TC heavy rains (Islam and Uyeda, 2005; Chen et al., 2013).

In summary, despite some discrepancies, the simulation reproduces reasonably well the track, intensity, wind, pressure field and distribution of precipitation.

5. Oscillations in the modeled TC Hagupit

5.1. *Analysis methods for the eyewall*

Model output from Domain 3, with a time interval of 15 minutes, is analyzed with a focus on 21–36 hours of model integration, when the TC intensity is highest and relatively stable. Vertical velocities, water vapor convection $[-w(\partial q/\partial t)$, where q is the water vapor mixing ratio], inward radial wind (IRW) and dry air density are averaged in the updraft region to examine the sequences of the high-frequency oscillations. Here, the definition of the updraft region and IRW are illustrated in Fig. 10. The updraft region is determined by the structure of the time-averaged secondary circulation of the TC shown in Fig. 10a. It is the vertical ascending motion area (with $w > 0$) extending from the TC center to a radius of 90 km. The IRW is determined by the TC's horizontal winds,

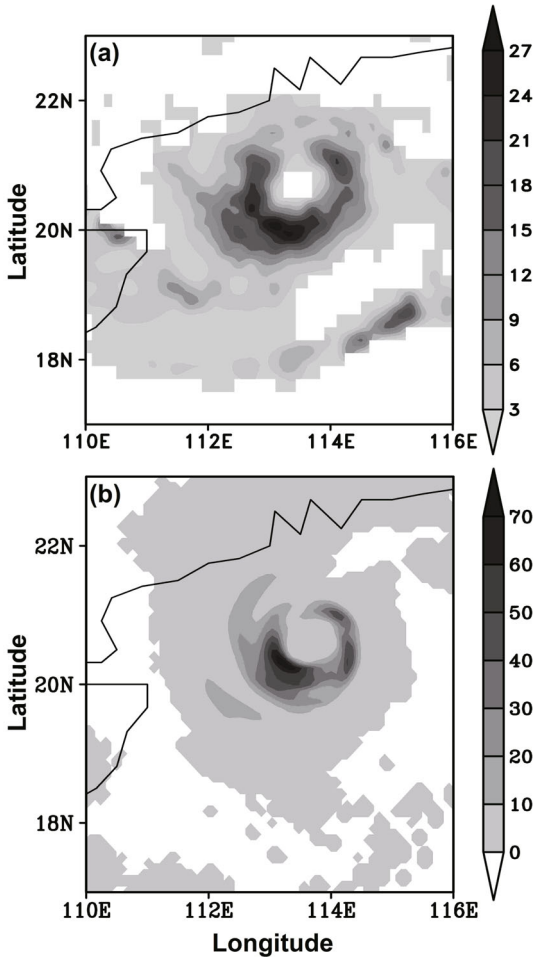

Fig. 9. Surface rain rates (mm h^{-1}) from (a) TRMM Microwave Imager (TMI) 2A12 at 1354 UTC and (b) the model simulation at 1400 UTC 23 Sep 23 (26 h of integration).

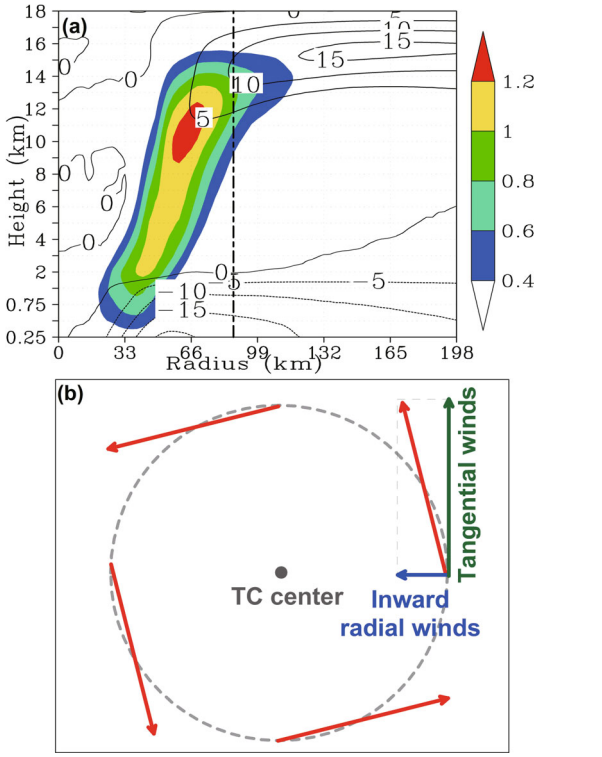

Fig. 10. (a) Radius–height distribution vertical velocities (m s^{-1}) averaged over time (21–36 h) and azimuthally. (b) Sketch of the definition of inward radial winds (IRW) in lower layers.

which can be divided into tangential and radial components. As shown in Fig. 10b, the IRW is directed toward the TC center. The calculation of water vapor convection is based on the equation for the condensation rate:

$$C - E = -u\frac{\partial q}{\partial x} - v\frac{\partial q}{\partial y} - w\frac{\partial q}{\partial z} - \frac{\partial q}{\partial t}\,, \tag{4}$$

where C is condensation and E is evaporation. Because most of the vapor concentrates in the boundary layer, the water vapor convection makes a dominant contribution to the condensation rate in the upper atmosphere.

Variables such as vertical velocity, water vapor convection, IRW and dry air density at a certain height and averaged over the updraft region, are analyzed through calculating their normalized departures and the NWPS.

Take the variable $A(x,y,z,t)(x = x_0, x_1, \ldots, x_X, y = y_0, y_1, \ldots, y_Y, z = z_0, z_1, \ldots, z_Z, t = t_0, t_1, \ldots, t_T)$ for example. It is first averaged in the updraft region at a certain height:

$$\overline{A}(z,t) = \frac{\sum_{x=x_1}^{x=x_X}\sum_{y=y_1}^{y=y_Y} A(x,y,z,t)}{X \cdot Y}\,, \tag{5}$$

where X, Y, Z, and T denotes the numbers of the grid points within the eyewall region. Then, $\overline{A}(z,t)$ is used to calculate the normalized departure and the NWPS for further analysis. The normalized departure $A'(z,t)$ is the departure of $\overline{A}(z,t)$ from its time-averaged value $\overline{\overline{A}}(z)$ divided by its standard deviation $\sigma(z)$, i. e.,

$$A'(z,t) = \frac{\overline{A}(z,t) - \overline{\overline{A}}(z)}{\sigma(z)}\,, \tag{6}$$

where $\overline{\overline{A}}(z)$ and $\sigma(z)$ are defined by

$$\overline{\overline{A}}(z) = \frac{\sum_{t=t_1}^{t=t_T} A(z,t)}{T}\,, \tag{7}$$

$$\sigma(z) = \sqrt{\frac{1}{T}\sum_{t=t_1}^{t=t_T}[A(z,t) - \overline{\overline{A}}(z)]^2}\,. \tag{8}$$

5.2. *Sequences of the high-frequency oscillations*

Figure 11 shows the normalized departure of vertical velocities, water vapor convection, IRW and air density calculated by Eq. (6). In Fig. 11a, an increase (decrease) of water vapor convection generally corresponds to an increase (decrease) of upward vertical motion, suggesting that convection is largely driven by upward motion. The upward motion contains significant high-frequency oscillations with periods of about 2 hours and propagating upwards. Figures 11b and c show that high-frequency oscillations also occur in IRW and air density.

Figures 11a–c also suggest that the oscillations of these variables follow a certain order. For example, a decrease of air density is usually followed by intensified convergence in the PBL, which enhances the upward motion at the top of the PBL. When strong upward motion reaches the height of 8–10 km, the MWS begins to increase and subsequently reaches its peak value. Based on CISK (conditional instability of second kind) theory, the strengthening of TC intensity is controlled by warming associated with condensation around the TC center (the warm core) of the upper layer, which is located at the height of 8–10 km (figure not shown). Because the water vapor convection controlled by upward motion makes a dominant contribution to the condensation rate, the TC intensity increases after strong upward motion reaches the height of the warm core.

Through examining the time series of high-frequency oscillations shown in Fig. 11, sequences of high (peak) and low (valley) values for these variables are identified. The results are summarized schematically in Fig. 12. In a typical cycle shown in the left column, the drop of density in the PBL is followed by an increase in IRW; this enhanced frictional convergence causes an increase in density, followed by a decrease in IRW. Next, we examine the consequence of the IRW increase, illustrated by the top row. The increase in convergence in the PBL causes an increase of updraft at the top of the PBL, followed by high vertical velocity at high altitudes of 8–10 km, and then an increase of the MWS. The consequence of the decrease in IRW in the PBL, shown in the bottom row, is the mirror image of that shown in the central column. The average time interval between two adjacent events is denoted by "Ave. Δt". The values of "Ave. Δt" in different boxes are all around 1.8 hours, suggesting that periods of oscillations for different variables are nearly the same.

Note that processes in the PBL are much more complex than those in the free atmosphere. For some events, variables in the PBL experience two high and low values in one cycle, while variables in the free atmosphere only have one high and low value in each cycle. Moreover, the times taken for differ-

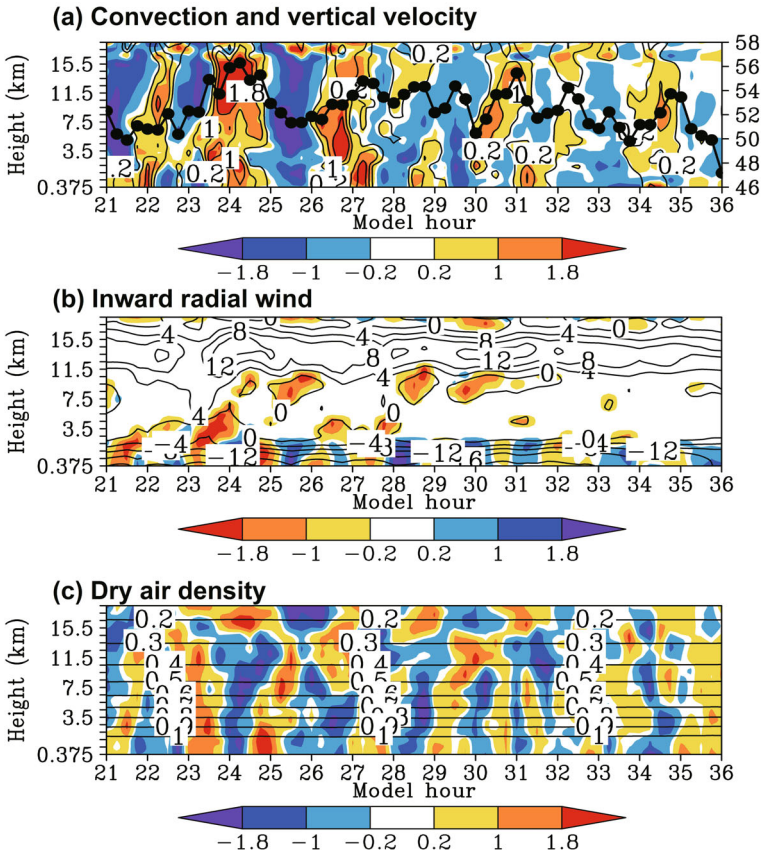

Fig. 11. Time–height variation of (a) convection and vertical velocity, (b) inward radial wind and (c) dry air density of the simulated Typhoon Hagupit (2008) averaged in the updraft region. In (a), contours show the normalized departure of vertical velocity of a certain height, and the color shading shows the water vapor convection $[-w(\partial q/\partial t)]$. The black curve with solid dots shows the maximum wind speed (right axis; units: m s^{-1}). In (b, c), contours show the original values of inwards radial winds (m s^{-1}) and dry air density (kg m^{-3}), respectively; the color shading shows its normalized departure. The standard deviations are computed for the variables at the same height.

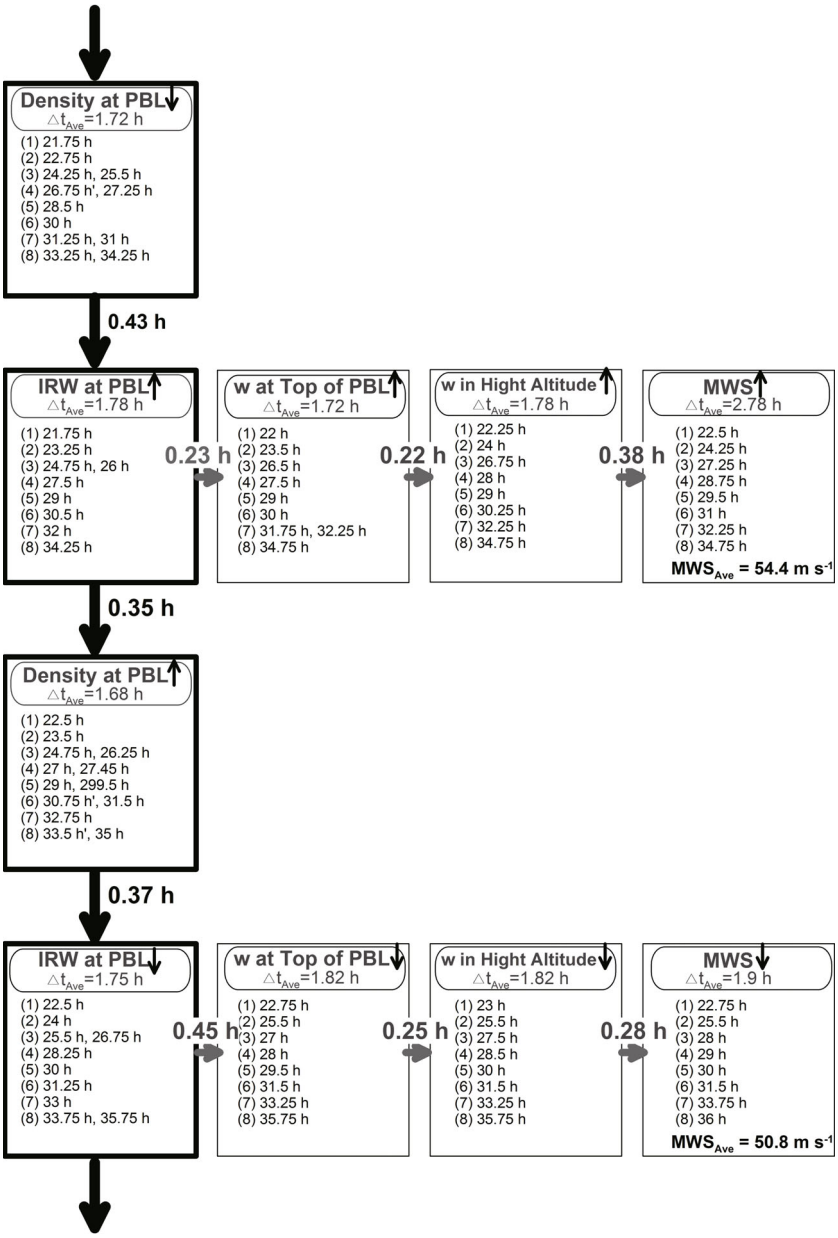

Fig. 12. The sequences of high-frequency oscillations in the simulated Typhoon Hagupit (2008). The variables shown are the vertical velocity (w), air density, IRW and maximum wind speed (MWS). Each box is for a particular variable reaching either its peak (denoted by "↑") or valley value (denoted by "↓"). The numbers in brackets [e.g. (1), (2), (3) etc.] indicate the event number identified from the time series shown in Fig. 5, followed by the model time when this event occurs. "PBL" denotes the planetary boundary layer, and "Δt_{Ave}" denotes the average time interval between two adjacent events. The sequences of the processes are denoted by thick arrows between two adjacent boxes, with the averaged time interval marked aside.

ent variables to increase/decrease is also different. In Fig. 12, an event number is assigned when a particular value starts to increase or decrease, and the values that follow are the model times when this value reaches the peak or valley. Because of differences in acceleration/deceleration, a variable that starts to increase/decrease earlier may reach its peak/valley behind another variable that starts to increase/decrease later. Hence, further statistical analysis is required to more accurately reveal the relationship among oscillations of various variables.

5.3. *The wavelet power spectrum*

The wavelet transform is applied to the vertical velocities at different levels, IRW and dry air density in the boundary layer and averaged in the updraft region, and the intensity of the simulated Typhoon Hagupit (2008). The analysis results are presented in Fig. 13. The high-frequency oscillations are

significant in all of these components, except for the central pressure. Surface pressure represents the total mass of the air column above the surface and its values change only slightly when the air within the column moves up and down. Hence, compared with winds, the surface pressure shows insignificant high-frequency oscillations.

As discussed in section 3, the period of 2 hours corresponds to a spatial scale of about 10 km for high-frequency oscillations. Based on the sequences of the high-frequency oscillations, this scale is related to the vertical depth of the updraft region of the TC and the radial range of the horizontal convergence area of the radial winds near the boundary layer (Fig. 10a).

Comparing Figs. 13a–c tells us that the oscillations of TC intensity lag those of other components by several hours. This suggests that it takes time for the TC intensity to respond to oscillations in the eyewall.

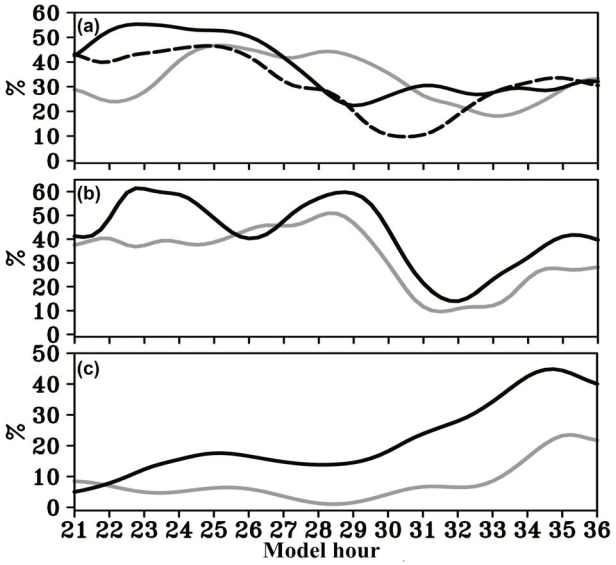

Fig. 13. The NWPS (units: %) integrated for variations at time scales of 90–150 minutes of the simulated (a) vertical velocities at different levels, (b) IRW (black) and dry air density (gray) in the boundary layer (0.625 km height) averaged in the updraft region, and (c) the maximum wind speed (black) and central pressure (gray) of the simulated Typhoon Hagupit (2008). In (a), gray-solid, black-dashed and black-solid lines represent the vertical velocity within the boundary layer (0.625 km height), at the top of the boundary layer (1.5 km height), and at high altitude (10 km height), respectively.

6. Conclusions and discussion

6.1. *Conclusions*

This paper reports the phenomenon of high-frequency oscillations in TCs. The observational evidence is obtained by applying the wavelet transform to the minutely wind speeds observed at Shangchuan Station during three TCs. At periods of about 2 hours, which corresponds to a scale of about 10 km, the spectral energy is significantly different from that of a red-noise process. The high-frequency oscillations are significant near the eyewalls and eyes of the TCs.

The simulation results for Hagupit (2008), during 15 hours when the TC intensity is highest and relatively stable, are analyzed. High-frequency oscillations are also found in the TC intensity, vertical motion, convective activity and air density. A visual inspection of the time series (Fig. 11) shows that the sequences of oscillations for different variables follow certain orders, which are summarized in Fig. 12. In a typical cycle, the drop of density in the PBL is followed by an increase in the IRW; this enhanced frictional convergence causes an increase in density, followed by a decrease in the IRW. The increase in convergence in the PBL causes an increase of updraft at the top of the PBL, followed by high vertical velocity at high altitudes of 8–10 km, and then an increase of the MWS, and vice versa.

6.2. *Discussion*

The relationships between the high-frequency oscillations and waves in the eyewall of TCs, such as the vortex Rossby waves, inertia gravity waves, and the fine-scale spatial rainbands, which are associated with Kelvin–Helmoltz instability and inertial-buoyancy waves, are worth discussing. On the one hand, because high-frequency oscillation is significant in variables averaged in the updraft region, this oscillation is a combination of large amounts of small-scale vortexes generated by the waves in the eyewall. On the other hand, both the high-frequency oscillations and waves in the eyewall affect the surface winds of the TC. The link between high-frequency oscillations and waves in the eyewall of TCs needs to explored in future studies.

Another question is what causes the density in the PBL to decrease after the IRW decreases. We speculate that a "trigger" mechanism may be at work, which is worthy of further study.

The present study mainly provides a descriptive picture of the high-frequency oscillations in TCs. The schematic summary provides a hint of the relationships among oscillations of different variables that deserves more in-depth investigation of the underlying dynamics, and the influences of these oscillations on TC intensities.

Acknowledgements. This work was supported by the National Natural Science Foundation of China (Grant Nos. 41375050, 41405048 and 41205032) and the China National Basic Research Program (Grant Nos. 2011CB403500 and 2014CB953904). We thank the two anonymous reviewers for their constructive comments on the original manuscript.

REFERENCES

Charney, J. G., and A. Elliassen, 1964: On the growth of the hurricane depression. *J. Atmos. Sci.*, **21**, 68–75.

Chen, Y., G. Brunet, and M. K. Yau, 2003: Spiral bands in a simulated hurricane. Part II: Wave activity diagnostics. *J. Atmos. Sci.*, **60**, 1239–1256.

Chen, Y., E. E. Ebert, K. J. E. Walsh, and N. E. Davidson, 2013: Evaluation of TRMM 3B42 precipitation estimates of tropical

cyclone rainfall using PACRAIN data. *J. Geophys. Res.*, **118**, 2184–2196, doi: 10.1002/jgrd.50250.

Christopher, T., and G. P. Compo, 1998: A practical guide to wavelet analysis. *Bull. Amer. Meteor. Soc.*, **79**, 61–78.

Davis, C. A., and S. Low-Nam, 2001: The NCAR-AFWA Tropical Cyclone Bogussing Scheme. A Report Prepared for the Air Force Weather Agency (AFWA). [Available online at http://www.mmm.ucar.edu/mm5/mm5v3/tc-report.pdf.]

DeMaria, M., C. R. Sampson, J. A. Knaff, and K. D. Musgrave, 2014: Is tropical cyclone intensity guidance improving? *Bull. Amer. Meteor. Soc.*, **95**, 387–398.

Dudhia, J., 1989: Numerical study of convection observed during the winter monsoon experiment using a mesoscale two-dimensional model. *J. Atmos. Sci.*, **46**, 3077–3107.

Emanuel, K. A., 1986: An air-sea interaction theory for tropical cyclones. Part I, Steady state maintenance. *J. Atmos. Sci.*, **43**, 585–605.

Emanuel, K. A., 1989: The finite-amplitude nature of tropical cyclogenesis. *J. Atmos. Sci.*, **46**, 3431–3456.

Emanuel, K. A., 1997: Some aspects of inner-core dynamics and energetic. *J. Atmos. Sci.*, **54**, 1014–1026.

Emanuel, K. A., 1999: Thermodynamic control of hurricane intensity. *Nature*, **401**, 665–669.

Emanuel, K. A., 2000: A statistical analysis of tropical cyclone intensity. *Mon. Wea. Rev.*, **128**, 1139–1152.

Hendricks, E. A., M. T. Montgomery, and C. A. Davis, 2004: The role of "vortical" hot towers in the formation of tropical cyclone Diana (1984). *J. Atmos. Sci.*, **61**, 1209–1232.

Hong, S.-Y., and J.-O. J. Lim, 2006: The WRF Single-Moment 6-Class microphysics scheme (WSM6). *J. Korean Meteor. Soc.*, **42**, 129–151.

Hong, S. Y., J. Dudhia, and S. H. Chen, 2004: A revised approach to ice microphysical processes for the bulk parameterization of clouds and precipitation. *Mon. Wea. Rev.*, **132**, 103–120.

Islam, Md. N., and H. Uyeda, 2005: Comparison of TRMM 3B42 products with surface rainfall over Bangladesh. *Proceedings in the IEEE International Geoscience and Remote Sensing Symposium* (IGARSS05), IEEE, Seoul, 412–415.

Kain, J. S., 2004: The Kain-Fritsch convective parameterization: An update. *J. Appl. Meteor.*, **43**, 170–181.

Kain, J. S., and J. M. Fritsch, 1990: A one-dimensional entraining/detraining plume model and its application in convective parameterization. *J. Atmos. Sci.*, **47**, 2784–2802.

Kain, J. S., and J. M. Fritsch, 1993: Convective parameterization for mesoscale models: The Kain-Fritsch scheme. *Meteor. Monogr.*, **24**, 165–170.

Ki, M. O., and H. Y. Chun, 2011: Inertia gravity waves associated with deep convection observed during the summers of 2005 and 2007 in Korea. *J. Geophys. Res.*, **116**(D16), doi: 10.1029/2011JD015684.

Knapp, K. R., and M. C. Kruk, 2010: Quantifying interagency differences in tropical cyclone best-track wind speed estimates. *Mon. Wea. Rev.*, **138**, 1459–1473.

Kurihara, Y., 1976: On the development of spiral bands in a tropical cyclone. *J. Atmos. Sci.*, **33**, 940–958.

Li, J. N., G. Wang, W. S. Lin, Q. H. He, Y. R. Feng, and J. Y. Mao, 2013: Cloud-scale simulation study of Typhoon Hagupit (2008). Part I: Microphysical processes of the inner core and three-dimensional structure of the latent heat budget. *Atmospheric Research*, **120–121**, 170–180.

Li, Q., Y. Duan, H. Yu, and G. Fu, 2010: Finescale spiral rainbands modeled in a high-resolution simulation of Typhoon Rananim (2004). *Adv. Atmos. Sci.*, **27**, 685–704, doi: 10.1007/s00376-009-9127-y.

Low-Nam, S., and C. Davis, 2001: Development of a tropical cyclone Bogussing Scheme for the MM5 system. The 11th PSU/NCAR Mesoscale Model User's Workshop, 130–134.

Menelaou, K., and M. K. Yau, 2014: On the role of asymmetric convective bursts to the problem of hurricane intensification: Radiation of vortex Rossby waves and wave-mean flow interactions. *J. Atmos. Sci.*, **71**, 2057–2077.

Mlawer, E. J., S. J. Taubman, P. D. Brown, M. J. Iacono and S. A. Clough, 1997: Radiative transfer for inhomogeneous atmosphere, RRTM, a validated correlated-k model for the longwave. *J. Geophys. Res.*, **102**, 16 663–16 682.

Montgomery, M. T., and R. J. Kallenbach, 1997: A theory for vortex Rossby-waves and its application to spiral bands and intensity changes in hurricanes. *Quart. J. Roy. Meteor. Soc.*, **123**, 435–465.

Montgomery, M. T., M. E. Nicholls, T. A. Cram, and A. B. Saunders, 2006: A vortical hot tower route to tropical cyclogenesis. *J. Atmos. Sci.*, **63**, 355–386.

Montgomery, M. T., N. V. Sang, R. K. Smith, and J. Persing, 2009: Do tropical cyclones intensify by WISHE? *Quart. J. Roy. Meteor. Soc.*, **135**, 1697–1714.

Reasor, P. D., M. T. Montgomery, F. D. Marks Jr., and J. F. Gamache, 2000: Low-wavenumber structure and evolution of the hurricane inner core observed by airborne dual-Doppler radar. *Mon. Wea. Rev.*, **128**, 1653–1680.

Romine, G. S., and R. B. Wilhelmson, 2006: Finescale spiral band features within a numerical simulation of Hurricane Opal (1995). *Mon. Wea. Rev.*, **134**, 1121–1139.

Rotunno, R., and K. A. Emanuel, 1987: An air-sea interaction theory for tropical cyclones. Part II: Evolutionary study using a nonhydrostatic axisymmetric numerical model. *J. Atmos. Sci.*, **44**, 542–561.

Schecter, D. A., 2008: The spontaneous imbalance of an atmospheric vortex at high Rossby number. *J. Atmos. Sci.*, **65**, 2498–2521.

Shapiro, L. J., and H. E. Willoughby, 1982: The response of balanced hurricanes to local sources of heat and momentum. *J. Atmos. Sci.*, **39**, 378–394.

Skamarock, W. C., and Coauthors, 2008: A description of the Advanced Research WRF Version 3, 1–113. [Available online at http://www.mmm.ucar.edu/wrf/users/docs/arw_v3.pdf.]

Wang, B., and J. C. L. Chan, 2002: How strong ENSO events affect tropical storm activity over the western North Pacific. *J. Climate*, **15**, 1643–1658.

Willoughby, H. E., 1976: Inertia-Buoyancy waves in hurricanes. *J. Atmos. Sci.*, **34**, 1028–1039.

Ying, M., W. Zhang, H. Yu, X. Lu, J. Feng, Y. Fan, Y. Zhu, and D. Chen, 2014: An overview of the China Meteorological Administration tropical cyclone database. *J. Atmos. Oceanic Technol.*, **31**, 287–301, doi: 10.1175/JTECH-D-12-00119.1

Zhong, W., D.-L. Zhang, and H.-C. Lu, 2009: A theory for mixed vortex Rossby-gravity waves in tropical cyclones. *J. Atmos. Sci.*, **66**, 3366–3381.

Zhu, P., J. A. Zhang, and F. J. Masters, 2010: Wavelet analyses of turbulence in the hurricane surface layer during landfalls. *J. Atmos. Sci.*, **67**, 3793–3805.